Microfluidic Serial Dilution Device for Multiplexed Microbial Chemotaxis Screening

by

Julia Noble

Senior Thesis, Mechanical Engineering

Tufts University

School of Engineering

Medford, Massachusetts

May 2, 2019

Thesis Advisor: Prof. Jeffrey S. Guasto

Thesis Committee: Prof. Behrouz Abedian

Acknowledgements

I would like to thank everyone who supported and contributed to this project. I would like to thank my research advisor, Prof. Jeffrey Guasto, for his continual guidance throughout the project. Sharing his vast knowledge on microfluidics and providing me with the necessary lab equipment enabled me to make the progress that I did. I want to thank Michael Stehnach for training me on the equipment and offering his help throughout the project. I am especially thankful for his photolithography fabrication work in the clean room and his help with the Matlab data analysis. I would also like to thank Prof. Behrouz Abedian for being a part of my thesis committee. This work was supported by a grant from the National Science Foundation (OCE-1829827) awarded to Prof. Jeffrey Guasto.

Abstract

Microbial chemotaxis is the directed movement of swimming cells toward favorable chemical cues including nutrients and signaling molecules. In particular, chemotaxis plays a crucial role in marine ecosystems by regulating biogeochemical processes such as carbon cycling. To untangle the web of microscale chemotactic interactions, the response of diverse bacterial species to a range of different chemical cues must be systematically screened across various chemical concentrations for multiple replicates. We engineered a rapid screening assay for bacterial chemotactic responses through the design and fabrication of a multiplexed microfluidic device. The device uses serial dilution to enable five simultaneous chemotaxis assays spanning five orders of magnitude in chemoattractant concentration plus a control assay. The performance of the serial dilution stage of the device was tested by measuring flow rates to determine relative dilution via particle tracking. Due to complications during the microfabrication process, we were unable to manufacture the intended dual height microchannel design, leading to a deficiency in performance. Combined with automated microscopy and further redesign, the device has the potential to reduce 960 individual chemotaxis assays down to just 32, vastly improving the efficacy of microbial screening.

List of Figures

Table of Contents

1.0 Introduction

The goal of this research was to create a microfluidic device that enables rapid and efficient screening of microbial chemotaxis across a wide array of dissolved chemical compounds and concentrations. In particular, this work is part of a broader study aimed at understanding marine bacterial chemotaxis's effect on carbon cycling but such a device could be applied to broader array of microorganisms and applications, including pharmaceutical development[1, 16].

Chemotaxis is the ability of bacteria and other microbes to detect chemical gradients and alter their motility to migrate toward the source of the chemical[14]. It is well known that marine bacterial chemotaxis plays a significant role in important ecosystem processes such as carbon fixation and nutrient cycling[3]. However, connections between the micro-scale process of viral-induced chemotaxis and its large-scale impact on the ecosystem remain unknown. The ultimate aim of our overarching project is to quantify the impact of viral-infected phytoplankton on cross-trophic level cell interactions. As a key step toward reaching this goal, we designed a microfluidic device for screening the chemotactic response of swimming marine bacteria to a host of chemoattractants as well as exudates from different virus infected bacteria. A single assay requires the ensemble statistics of cell motility of several thousand bacteria within a well-defined gradient, where microfluidics provides a state-of-the-art approach[3]. Since the degree to which bacteria respond to chemicals is highly dependent on the magnitude of the chemical gradient[1], we aim to observe chemotaxis under 5 different chemical gradient strengths. To collect sufficient data on marine bacterial chemotaxis, approximately four different species of bacteria must be tested against eight different chemoattractants under five different chemical gradient strengths in addition to one control gradient and with three to five replicates each. These experiments amount to 480-960 individual chemotaxis assays. To more rapidly perform the vast number of chemotaxis assays required, the microfluidic device uses serial dilution[10,15] to create five

different chemical gradients plus a no-gradient control to quantify bacterial chemotactic responses. With this serial dilution device, six different chemotaxis tests across a range of chemical gradient strengths can be performed at once without the need to manually generate each gradient. Combined with automated microscopy to perform replicate experiments, this device will significantly reduce the time to collect the necessary chemotaxis data.

2.0 Background

Bacteria often swim in random walk motility patterns using flagellar appendages for both propulsion and turning. In the presence of a chemical gradient, cells bias this random walk to migrate up or down a chemical gradient toward an attractant or repellent, respectively. The stronger the chemical gradient, the stronger the response from chemotactic microbes[1]. With the advantage of chemotaxis, microbes can migrate towards areas with more favorable living conditions[2]. By combining efficient steering and fast swimming, microbes can effectively utilize chemotaxis to gain physical advantages in colonizing host animals, locating biogenic particles, attaching to surfaces, and maintaining position next to phytoplankton cells[22]. On a larger scale, research suggests that chemotactic behavior of microbes boosts major environmental cycles, such as the carbon cycle and the nitrogen cycle[3, 25].

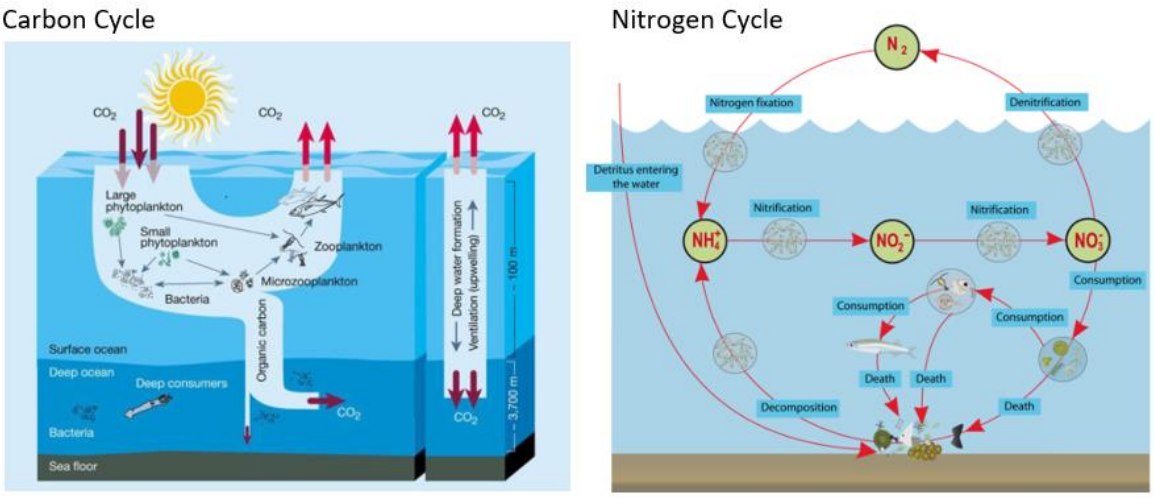

Figure 1: The carbon cycle (left)[23] and the nitrogen cycle (right)[24] within the ocean.

2.1 The Environmental Importance of Chemotaxis

Evidence suggests that chemotaxis enhances the carbon cycle[3, 25], an essential process of the ecosystem where carbon compounds are interconverted in the environment and exchanged among the ocean, air, and land[4]. Marine bacteria play a role in carbon-cycling by influencing the amount of carbon retained within the upper ocean[3]. Marine bacteria process the carbon that sinks into the ocean[3]. The more carbon that the marine bacteria process, the more carbon dioxide the ocean can absorb from the air[3]. Chemotaxis improves marine bacteria's ability to move towards the dissolved carbon in the ocean, known as dissolved organic carbon (DOC), to be interconverted[3]. Chemotactic marine bacteria swim toward areas of high DOC concentration, which increases the amount of carbon processed by marine bacteria[3]. Theoretical mathematical models predict that chemotaxis can double marine bacterial uptake of carbon at points of high DOC concentrations, where chemotactic marine bacteria congregate[3].

Marine bacteria also have multiple roles in the nitrogen cycle, an ecological process that coverts nitrogen into various nitrogen compounds as it circulates through the environment. Nitrogen is a critical nutrient for all living organisms. However, most of the nitrogen in the environment is in the form of dinitrogen gas, which is not a form of nitrogen that plants and animals can use[6]. Within the nitrogen cycle via ammonification, bacteria convert the dinitrogen gas into ammonia, the accessible form of nitrogen for plants and animals[5]. Other bacterial-facilitated nitrogen cycle processes include nitrification, the conversion of ammonia to nitrites and nitrates[7], and denitrification, the conversion of nitrites and nitrates to nitrogen gas[8]. Chemotaxis enhances these steps of the nitrogen cycle. Chemotactic marine bacteria respond to gradients of ammonia, nitrates, nitrites, and oxygen, which allows chemotactic marine bacteria to move toward and stay within areas favorable for ammonification, nitrification, and

denitrification[3]. Chemotaxis increases productivity in the nitrogen cycle and, in turn, supports the marine ecosystem. Without chemotactic microbes, ammonia, the critical animal and plant nutrient, would be more of a scarcity.

While chemotaxis is generally known to be an important part of the carbon cycle and nitrogen cycle, viral infections in microbes can augment or induce chemotaxis among bacteria. This process and its environmental impact on carbon cycling are not well understood. For viral-induced chemotaxis, the bacteria-attracting chemicals, called chemoattractants[17, 26], are exudates usually produced by non-motile, virus infected bacteria. These exudates include a variety of substances such as amino acids, simple sugars, and carbon[25]. The exudates seep out of the virus infected bacterium and attract other motile chemotactic bacteria, which take up exudates as nutrients through osmosis (osmotrophs), as shown in Fig. 2. Such chemical signals can also enhance the predation of bacteria by attracting larger single celled or multicellular organisms. To fully understand the role of viral infections in upper ocean carbon-cycling, more research on chemotaxis toward virus infected microbes is necessary.

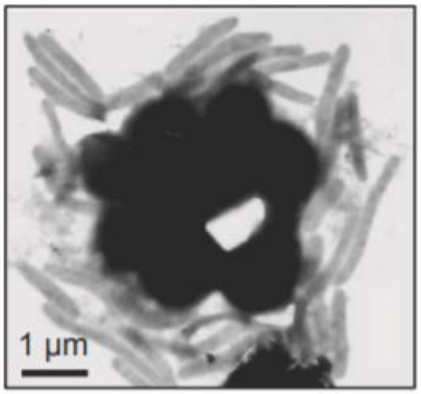

Figure 2: Cellulophaga, chemotactic marine bacteria, gather around an infected photobacterium.[30]

2.2 Limitations of Existing Chemotaxis Assays and Microfluidic Devices

Chemotaxis assays are laboratory experiments that test the response of motile bacteria to an imposed chemical gradient[18] and are typically performed with microfluidic devices[27, 28, 29, 36]. By performing such assays, the degree to which a species of bacteria is attracted (or repelled) to a specific chemoattractant can be determined[18]. Since stronger chemical gradients elicit stronger chemotactic reactions, chemotaxis assays are commonly performed in sets of several different chemical gradients.

One of the simplest ways to perform a chemotaxis assay is with a T-junction microfluidic device. This chemotaxis device uses a "T"-shaped intersection of channels, as shown in Fig. 3, consisting of two inlet channels that converge into a single outlet channel. A solution containing the chemoattractant is pumped into one of the inlet channels, while a solution containing the chemotactic bacteria is pumped into the other inlet channel. When the two channels converge into one outlet channel, the attractant slowly diffuses across the channel, which creates a chemical gradient as the fluid flows down the channel. With this setup, the chemotactic bacteria are free to swim to the chemoattractant side within the outlet channel. A variation on this assay involves abruptly stopping the flow in the channel to observe the temporal evolution of the bacterial distribution in the evolving attractant gradient. The number of bacteria that swim toward the chemoattractant side of the channel determine how strongly the bacteria react to the chemoattractant.[9]

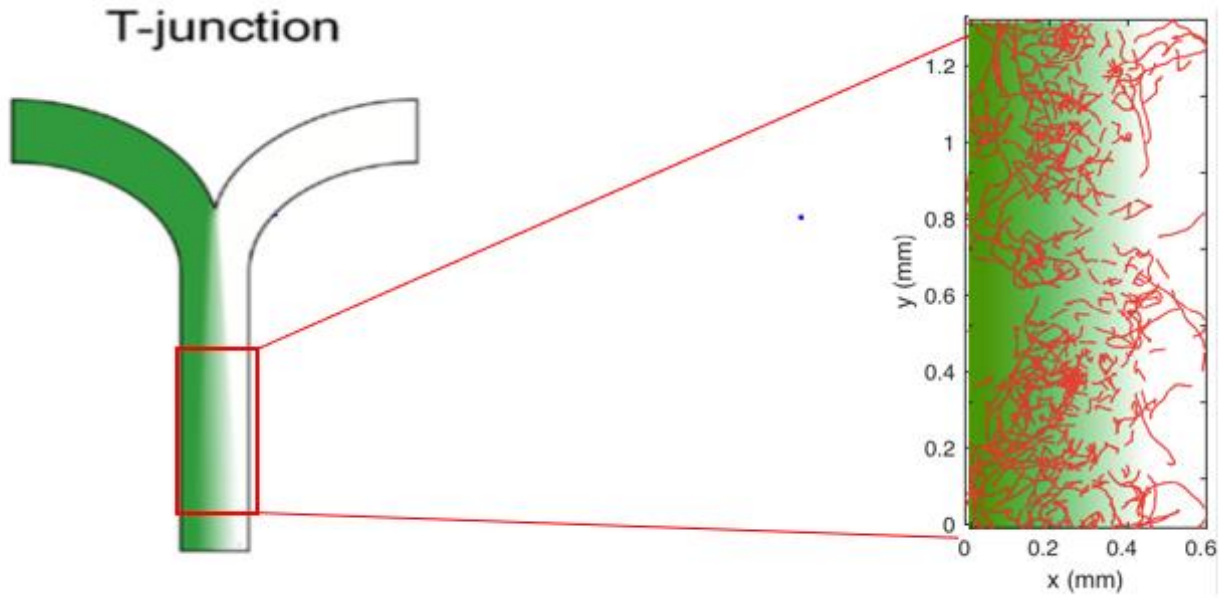

Figure 3: A T-junction microfluidic device. The green represents the concentration of chemoattractant and the white represents the solution containing the bacteria (left)[9]. The tracked paths of chemotactic marine bacteria within a channel showing a greater number of bacteria on the chemoattractant side (right) (credit: Michael Stehnach).

The T-junction channel device is limited in that it can only perform a single chemotaxis assay at a time. Additionally, the desired concentration of chemoattractant to be tested must be manually created via pipetting. Both of these drawbacks make the classic single T-junction microchannel too time-consuming and tedious to test a wide variety of bacterial species, chemoattractants, and chemical concentrations.

Various microfluidic devices, such as the µflow Device[27] and the SlipChip[36], have been developed as improvements of the basic T-junction chemotaxis assay. The µflow Device (Fig. 4) creates a more predictable and customizable concentration gradient than the T-junction device. The serpentine channels of the µflow Device form 8 different concentrations via diffusive mixing. The concentrations are then combined to create a very stable concentration gradient to perform the chemotaxis assay under. The same method for analyzing T-junction assays is used for analyzing the µflow Device assays.[27]

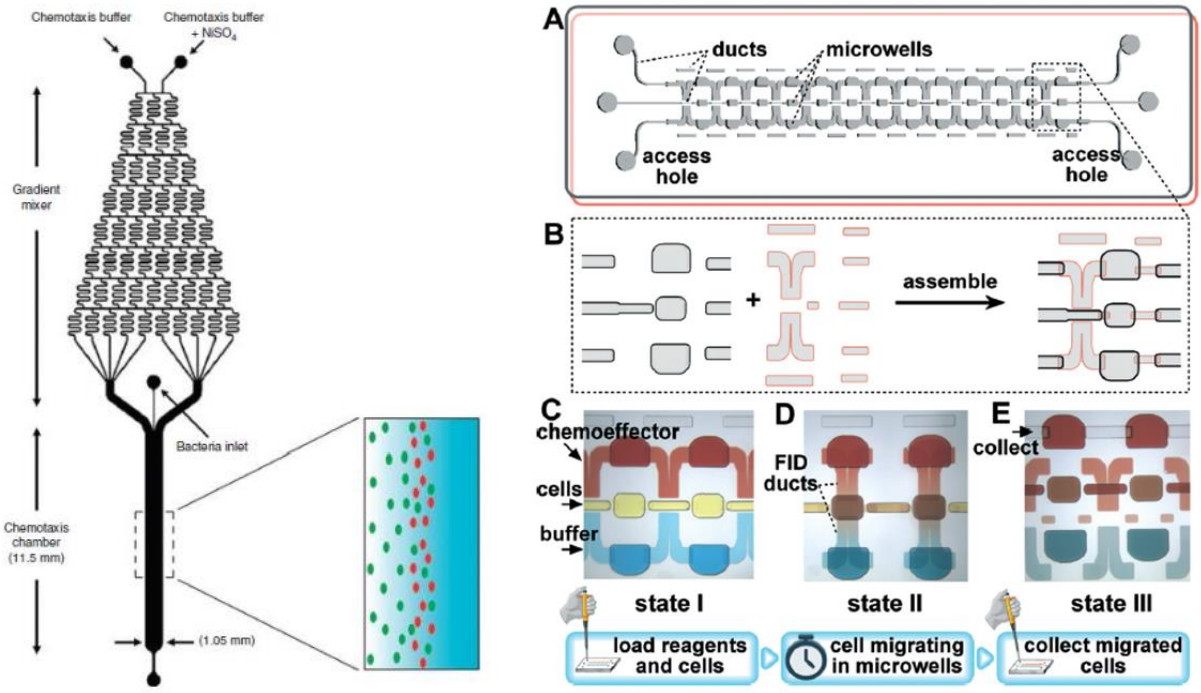

Figure 4: The µflow Device (left)[27] and the SlipChip with (A) schematic illustration, (B) close-up of the assembly of top and bottom plates, and (C) step-by-step procedure demonstrated by food dye (right)[36].

The SlipChip (Fig. 4) provides a quick method for performing several chemotaxis assay replicates at once. The SlipChip consists of two glass plates with 3 sets of wells etched into the bottom plate and well connector channels etched into the top plate. Bacteria are placed in the middle set of wells. Chemoattractant fills another set of wells to the side of the bacteria wells, and buffer fills the set of wells on the opposite side of the bacteria wells. The chemotaxis assay is performed by sliding the top chip across the bottom chip, connecting the wells together with microchannels. Once the wells are connected, the bacteria are free to swim from the bacteria well to either the buffer well or the chemoattractant well. The bacteria are collected at the end of the experiment by sliding the top plate of the SlipChip a second time, closing off the exits of the wells. The SlipChip chemotaxis assay is analyzed by determining how many bacteria swam into

the chemoattractant wells. The SlipChip can setup up to 20 duplicate chemotaxis units in parallel for quick collection of replicate test data.[36]

Although the µflow Device and SlipChip are more advanced chemotaxis assay tools than the T-junction Channel, both devices are unable to perform several different chemotaxis assays at once without significant manual preparation. The SlipChip can perform multiple assays at once, but only assays of the same chemical concentration. Without the ability to perform a variety of chemotaxis assays at once, the µflow Device and SlipChip fall short of efficiently performing the hundreds of different chemotaxis assays desired.

3.0 Design of Device

To overcome the shortcomings of the current chemotaxis assay devices, we based our device design concept on serial dilution with multiplexed T-channel chemotaxis assays for more efficient data collection in chemotaxis assays. In this thesis, we focus primarily on the serial dilution module design, where we adapted Hattori and his co-workers' approach to microfluidic serial dilution[10] for chemotaxis assay purposes. Our serial dilution module has one outlet and two inlets: one inlet for the base chemoattractant solution and the other for cell media (buffer). The device was designed to be used with a pressure regulated source. The microchannels within the device parse out the chemoattractant and divert it to an array of observation channels after a step-wise (serial) dilution. During chemotaxis assays, the device is observed under a microscope (Fig. 5).

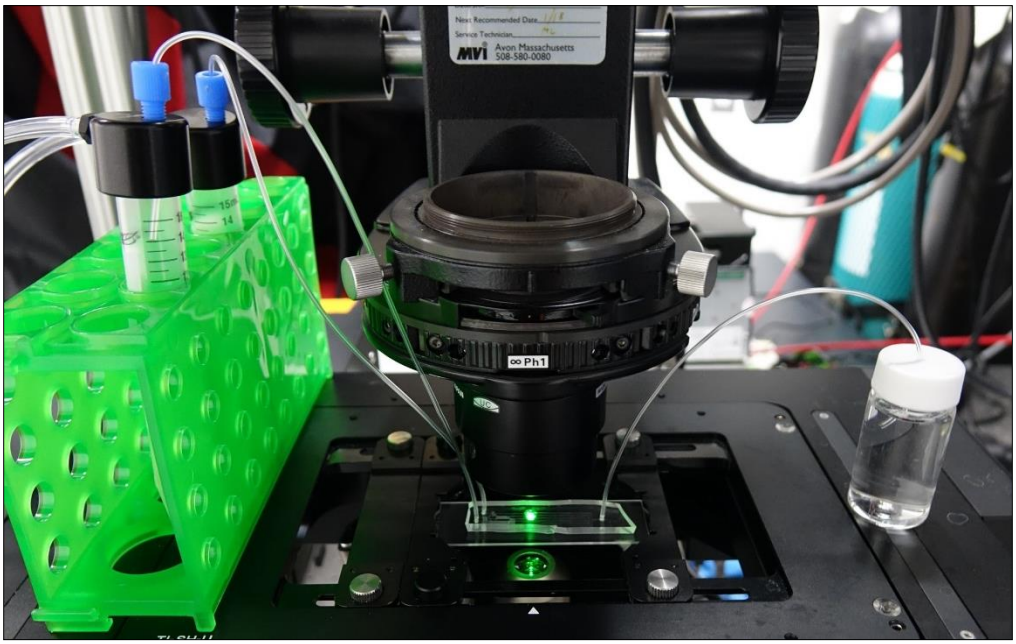

Figure 5: The serial dilution device (center) set up under a microscope. The inlets are connected to the chemoattractant solution and buffer (left), which are driven by a pressure controller, and the outlet is connected to a waste bin (right).

3.1 Advantages of On-chip Serial Dilution

The device was designed to create five different concentrations from the base chemoattractant solution within five of the 6 observation channels of the device via serial dilution. The sixth branch was designed to contain buffer to serve as an experimental control. Serial dilution is a method of proportionally diluting a substance in a solution in a stepwise manner. The solute is diluted in proportion to a set dilution factor. The resulting solution is then diluted again – in this case, with the same dilution factor - to further reduce the concentration of the solute in solution. This proportional dilution is then successively repeated using less and less concentrated solutions until the desired concentration (or series of concentrations) is achieved. The serial dilution results in a series of logarithmically decreasing concentrations as shown in Fig. 6. For the serial dilution device designed here, we chose a constant dilution factor of 10. In other words, the chemoattractant solution was diluted with buffer in a ratio of 1:9. The resulting solution was

subsequently diluted with buffer in a ratio of 1:9 four more times in the same manner. The relative concentrations resulting from serial dilution with a dilution factor of 10 were 1, 10^{-1}, 10^{-2}, 10^{-3}, and 10^{-4}. By creating a multiplexed device with the ability to test chemotaxis under five different concentrations in addition to a control solution, we combined several assays into one. With serial dilution, the device can carry out 6 chemotaxis assays at once, significantly reducing preparation and setup time for such assays.

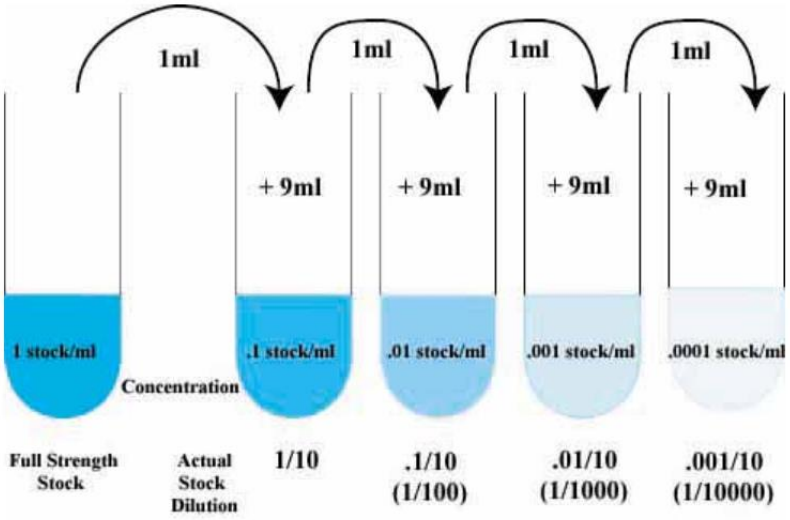

Figure 6: A serial dilution with a 1:9 ratio of substance of a solution to water buffer.[31]

The serial dilution in the device was carried out via a microchannel network. The microchannels were arranged so that part of the base concentration of attractant (c = 1) was diverted to the first test channel, while the remaining attractant was diverted toward the remaining test channels. The attractant stream is diluted by a factor of 10 by combining the attractant flow with the intersecting channel containing buffer (c = 0) at a flow rate that is 9 times greater than that of the attractant flow rate. The outflow channel stemming from this intersection thus has a chemoattractant solution diluted by a factor of 10 (c = 0.1). The dilution cycle now

begins again, where part of the resulting attractant stream is diverted to the second chemotaxis assay test channel, and the remainder is further diluted (i.e. to c = 0.01) as described above. This channel set up is repeated for 5 of the six observation channels. Fully concentrated attractant (c = 1) flows into the first observation channel and a pure water buffer (c = 0) flows into the sixth observation channel. Thus, the desired relative chemoattractant concentrations of the test channels are c = 1, 0.1, 0.01, 0.001, 0.0001, and 0.

3.2 Calculating the Appropriate Flow Rates of the Device

To calculate the appropriate flow rates for producing the desired chemoattractant concentrations of 1, 0.1, 0.01, 0.001, 0.0001, and 0, the flow rates were evaluated at each channel intersection. At the dilution intersections (nodes), where the buffer dilutes the attractant solution at a dilution factor of 10, the general form of the equations is:

$$9q_{solution} = q_{buffer} \qquad \text{(eq. 1)}$$

where $q_{solution}$ is the flow rate of the inlet channel branch containing the chemoattractant solution and q_{buffer} is the flow rate of the second inlet channel branch containing buffer.

The rest of the flow rate equations were derived from conservation of mass of incompressible flow. The conservation of mass for fluid dynamics states[32]:

$$\dot{M} = \rho_i v_i A_i - \rho_0 v_0 A_0 = \rho_i q_i - \rho_0 q_0 \qquad \text{(eq. 2)}$$

where $\dot{M}$ is the overall change in mass, ρ_i is the density of the incoming flow, ρ_0 is the density of the outgoing flow, v_i is the area-averaged velocity of the incoming flow, v_0 is the area-averaged velocity of the outgoing flow, and A_i is the cross-sectional area of the incoming flow channel, A_0 is the cross-sectional area of the outgoing flow channel, and q_i and q_0 are the volume flow rates of the incoming flow and outgoing flow respectively.

Because all the channels in which serial dilution takes place have equal fluid densities (incompressible) and the rate of change in mass is zero, equation 2 can be expressed in terms of the flow rates for each channel node:

$$\sum q_i = \sum q_0 \qquad \text{(eq. 3)}$$

where q_i are the flow rates of any fluids entering the channel intersection (the node) and q_0 are the flow rates of any fluids exiting the channel intersection. The flow rates of the microfluidic channels are analogous to the electric currents in an electric circuit. With Kirchhoff's circuit law, the electric currents at each node are summed in a similar manner to the flow rates of the nodes of the microfluidic channels in eq. 3[11].

The equations derived for each of the nodes within our serial dilution device schematic (Fig. 7) were combined with the dilution intersection equations to create a system of equations that was solved to calculate the flowrate of every channel in the schematic. The inlet channel pressures, P_1 and P_2, were set to 1 kPa and the observation channel flow rates, q_0, were set to 1µl/min. The rest of the flow rates were then solved with the system of equations (See Appendix A). The results are shown in table 1.

Table 1: The flow rates necessary for the serial dilution.

Label	Flow Rate (µl/min)
q0	1.000
q01	1.111
q11	1.000
q21	0.999
q31	0.990
q41	0.900
q12	1.111
q22	1.110
q32	1.100
q04	0.111
q14	0.111
q24	0.110
q34	0.100

These flow rate calculations were checked by recursively evaluating the following flow rate serial dilution equations[10] in Matlab:

$$q_{k,4} = \frac{C(k+1)}{C(k)} \sum_{i=k+1}^{N} \left(\frac{C(i)}{C(k)}\right) q_0 \ (\mathrm{k} = 0, 1, \ldots \mathrm{N}) \qquad \text{(eq. 4)}$$

$$q_{k,2} = \sum_{i=k}^{N} \left(\frac{C(i)}{C(k)}\right) q_0 \ (\mathrm{k} = 0, 1, \ldots \mathrm{N}) \qquad \text{(eq. 5)}$$

$$q_{k,1} = \frac{C(k-1) - C(k)}{C(k-1)} \sum_{i=k}^{N} \left(\frac{C(i)}{C(k)}\right) q_0 \ (\mathrm{k} = 0, 1, \ldots \mathrm{N}) \qquad \text{(eq. 6)}$$

where $C(k)$ is the final concentration in the kth microchannel branch, q_0 is the flow rate in the observation channels, $q_{k,4}$, $q_{k,2}$, $q_{k,1}$, are the flow rates in the kth microchannel branch of the connecting channels, diffusion mixing channels, and inlet side resistance channels respectively. N is the number of steps of the serial dilution; In our serial dilution device's case, N is 4. The flow rate results from this method matched the matrix equation results, independently confirming the flow rate values.

3.3 Modeling Microfluidic Channels with Ohm's Law

To create the necessary flow rates needed for serial dilution listed in table 1, the network of channels within the device was modeled as an electric circuit using Ohm's Law as shown in Fig. 7. For electric circuits, Ohm's law is:

$$\Delta V = i R_{Electric} \qquad \text{(eq. 7)}$$

with ΔV as the voltage difference across the circuit, i as the electric current, and $R_{Electric}$ as the electrical resistance. Ohm's law equation can be used to solve for the necessary electrical

resistances within an electrical circuit, given voltage drops and currents. We can make an analogy to Ohm's law for fluidic circuits to calculate the necessary fluidic resistances in our channel given the pressure drops and flow rates[11, 12]. With this analogy, Ohm's law takes the form[11, 12]:

$$\Delta P = qR_f \qquad \text{(eq. 8)}$$

where ΔP is the pressure drop across a channel, q is the flow rate within the channel, and R_f is the fluidic resistance of the channel. For reference, in the simple case of a circular channel, the fluidic resistance increases with viscosity and length, and decreases with increasing channel radius[12]. Equation 8 is only valid for low Reynolds number (Re) flow (Re <<1)[12]. Microfluidic flows are largely relegated to the low Re regime due to the relatively small length scales[33]. Typically, the Re in microfluidics is on the order of 1 or lower[33], placing the flows well within the laminar regime. In the case of the serial dilution device, Re was estimated to be around 2.8e-10 from the Reynolds number equation[34]:

$$Re = \frac{\rho v_0 h}{\eta} \qquad \text{(eq. 9)}$$

where ρ is the fluid density, η is the dynamic viscosity, h is the height of the channel (the characteristic length), and $q_0$is the flow velocity (the outlet channel flow rate was used for our Re estimate). Since Re is much less than 1, equation 8 is valid for our application.

The fluidic resistances of the circuit were solved for in a similar manner to solving for the flow rates previously found. Ohm's law equations for each branch were set up with set inlet and outlet pressures and known flow rate values. The fluidic resistance was then solved for with

a system of equations (See Appendix A).

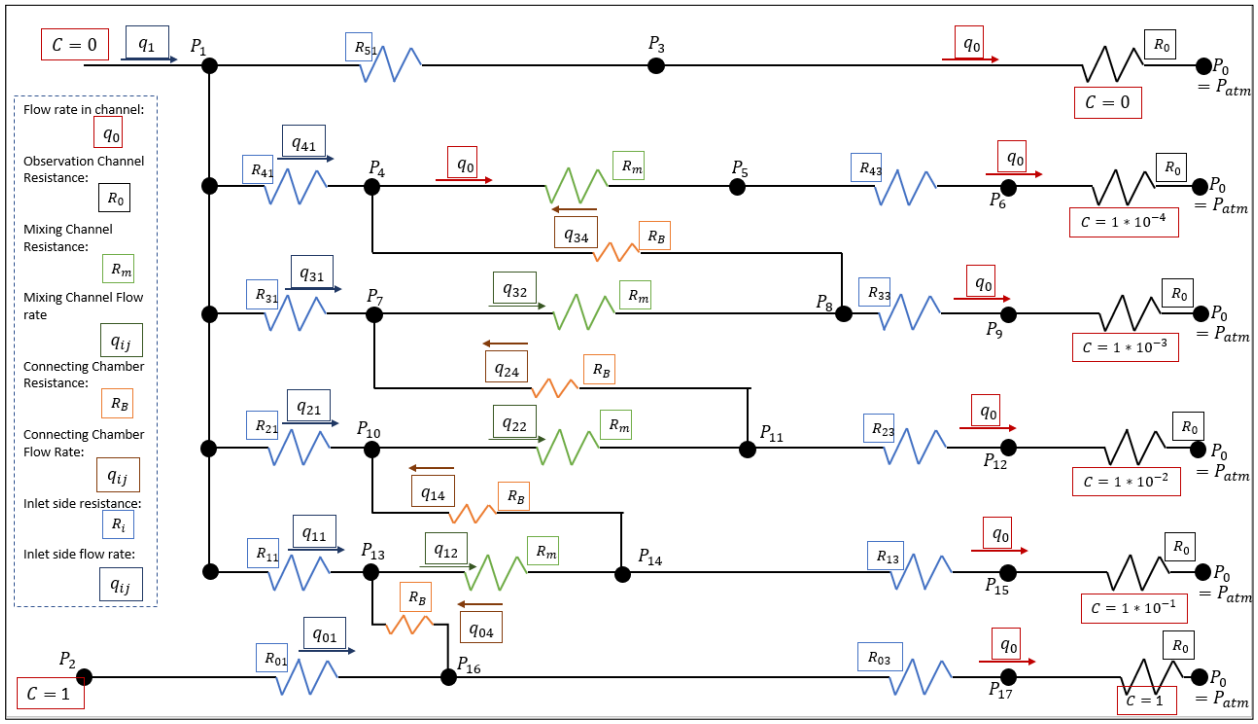

Figure 7: The serial dilution device schematic, modeled as an hydraulic circuit. Key is shown on the left.

The resulting resistance values were confirmed by the following equations for fluidic resistances in a serial dilution[10]:

$$R_{k,1} = \frac{(P_{in} - q_{k,3}R_{k,3})}{q_{k,1}} \ (k = 0,1 \dots N) \qquad \text{(eq. 10)}$$

$$R_{k,3} = \frac{(q_{k,4}R_{k,4} - q_{k+1,3}R_{k+1,3})}{q_{k,3}} \ (k = 0,1 \dots N-1) \qquad \text{(eq. 11)}$$

where $R_{k,1}$, $R_{k,3}$, and $R_{k,4}$ are the fluidic resistance in the kth inlet-side microchannels, outlet-side microchannels, and connecting microchannels respectively and P_{in} is the pressure at the inlet microchannels. N is again the number of steps in the serial dilution.

The matrix equation results and the Matlab equation results matched. The results for fluidic resistances necessary to perform the serial dilution are in table 2.

3.3 Calculating Channel Lengths Based on Fluidic Resistances

The dimensions of the channels were designed based off the calculated fluidic resistance values and the following equation relating the channel dimensions to fluidic resistance for a rectangular channel[11]:

$$R_f = \frac{12\eta L}{wh^3\left(1 - \frac{h}{w}\left(\frac{192}{\pi^5}\sum_{n=1,2,5}^{\infty}\frac{1}{n^5}\tanh\left(\frac{n\pi w}{2h}\right)\right)\right)} \qquad \text{(eq. 12)}$$

where R_f is the fluidic resistance of the channel, η is the dynamic viscosity, and h, w, and L are the height, width, and length of the channel respectively.

For the observation channel dimensions, we chose a fixed height of 100 μm and width of 750 μm, dimensions that were adequate for observing chemotaxis and did not inhibit bacterial motility. From these dimensions, the fluidic resistance of the observation channels was calculated. The fluidic resistance of the observation channels was accounted for in the rest of the device design by subtracting the observation channel fluidic resistance from the calculated fluidic resistance values of the outlet side microchannels ($R_{k,3}$, and $R_{5,1}$ in Fig. 7). We chose 50 μm for the width all channels excluding the observation channels and 15 μm for the height of all channels excluding the observation channels and the mixing channels. We chose these dimensions because they were fabricable dimensions that resulted in reasonably compact channel lengths that would fit on a standard glass microscope slide (25mm x 75 mm). Using equation 12, the length of each channel was calculated with the chosen width and height dimensions, the known fluidic resistance values (Table 2) and η set to the dynamic viscosity of water (See Appendix A). Different dimensions were chosen for the mixing channels to optimize mixing time and for the observation channels to enable clear observation of the chemotaxis assays.

In addition to calculating the appropriate channel lengths for creating the desired flow rates, we had to ensure that the diluted attractant streams appropriately mixed. To ensure that the attractant solution homogenously mixed with the buffer, we chose the mixing channel length to be just long enough for the attractant solution and the buffer to completely diffuse together. The approximate time for complete mixing via diffusion is[13]:

$$t_{mix} \approx \frac{l_{st}^2}{D} \qquad \text{(eq. 13)}$$

where t_{mix} is the time until complete diffusion and D is the diffusion coefficient. l_{st} is the distance over which diffusion must act to fully mix the concentration[13]. In the case of this serial dilution device, l_{st} is the width of the mixing channel. We combined equation 13 with the following two equations to calculate the mixing channel length necessary for create a homogenous solution via diffusion:

$$u = \frac{q}{hw} \qquad \text{(eq. 14)}$$

$$L_{mix} = ut_{mix} \qquad \text{(eq. 15)}$$

where u is the average flow speed, q is the flow rate through the mixing channel, and L_{mix} is the minimum channel length needed for complete mixing. Combining equations 13, 14, and 15 gives:

$$L_{mix} = \frac{qw}{hD} \qquad \text{(eq. 16)}$$

1.111 µl/min, the fastest flow rate within the mixing channels, was used for q in equation 16 to give an upper bound for the required mixing length. 5.62×10^{-10} m^2/s, the diffusion coefficient for calcein[10], was used as the diffusion coefficient. Since the mixing length is inversely proportional to the height of the channel, we made the mixing channels much taller than the other channels to

decrease the necessary length of the mixing channels. The diffusion length could also be minimized by decreasing the width of the mixing channel. However, this approach was avoided as all channels were fabricated at the minimum size given the resolution of our photolithography. The dimensions of the mixing channels are listed in table 2.

A dual-height channel network such as this one requires a two-layer fabrication approach, which adds significant complexity to the fabrication process. However, the dual-height network appears necessary for creating mixing channels that both mix the diluted attractant properly and are short enough to fit within the rest of channel network. The final channel dimensions are listed in table 2.

All the length values excluding the mixing channels and observation channels were checked using the approximation equation for the fluidic resistance of rectangular microchannels[11]:

$$R_f = \frac{12\eta L}{wh^3(1 - 0.63(\frac{h}{w}))} \qquad \text{(eq. 17)}$$

The above approximation is only accurate for rectangular microchannels with high aspect ratios (e.g. h/w << 1)[11]. This approximation is appropriate for our device since the channel width is much greater than the channel height which gives a high aspect ratio (h/w = 0.3). The values calculated from this approximation matched closely with our values calculated with equation 12, further confirming that the dimension lengths should provide the correct amount of fluidic resistance within the device.

Both equation 12 and equation 17 were confirmed as accurate methods of calculating the channel dimensions by comparing it to resistance and channel dimensions listed in Hattori[10].

Table 2: The fluidic resistances of the channels and the corresponding channel dimensions of the device.

Channel	Total Resistance (mPa-s/μm³)	Resistance minus $R_{observation}$ (mPa-s/μm³)	Depth (μm)	Width (μm)	Length (mm)	Length (μm)
R_m	0.0231	0.0361	100	50	16.475	1.648E+04
R_b	0.1000	0.1000	15	50	1.140	1.140E+03
R_{01}	0.5461	0.5461	15	50	6.228	6.228E+03
R_{11}	0.6180	0.6180	15	50	7.048	7.048E+03
R_{21}	0.6296	0.6296	15	50	7.180	7.180E+03
R_{31}	0.6465	0.6465	15	50	7.373	7.373E+03
R_{41}	0.7222	0.7222	15	50	8.236	8.236E+03
R_{51}	1.0000	0.9997	15	50	11.400	1.140E+04
R_{03}	0.3932	0.3929	15	50	4.481	4.481E+03
R_{13}	0.3821	0.3818	15	50	4.354	4.354E+03
R_{23}	0.3710	0.3707	15	50	4.227	4.227E+03
R_{33}	0.3600	0.3597	15	50	4.102	4.102E+03
R_{43}	0.3500	0.3497	15	50	3.988	3.988E+03
$R_{observation}$	0.0003	0.0000	100	750	15.000	1.500E+04

4.0 Microfabrication

The microfluidic device consists of a glass slide attached to a micro-molded block of polydimethylsiloxane (PDMS), in which the microfluidic channel network is imprinted. We fabricated the device with multi-layer photolithography, a process of transferring geometric shapes from a photomask onto a silicon wafer[19] in a thin layer of photoresist, and PDMS soft lithography, a process that casts PDMS with a photoresist mold on a silicon wafer[20].

The multi-layer photolithography was completed in two stages following the standard photolithography protocol from MicroChem Corp. For the first layer, the silicon wafer was spin-coated with SU-8 2010 (MicroChem Corp.), a high contrast epoxy-based photoresist. The photoresist was spun down to a uniform 15 micron-thick layer using a spin coater (Laurell WS-400B-6NPP-Lite Manual Spinner, Laurell Technologies Corp). The wafer with the 15-micron layer of photoresist was soft baked and then exposed to UV-light using a mask aligner (OAI Model 204IR Mask Aligner, OAI). Immediately after UV-light exposure, we post-baked the wafer and then developed it with SU-8 developer. Typically for multi-layer photolithography, the photoresist is only developed after the last layer has been applied[21]. However, since the channels were so small and difficult to see pre-development, the first layer of photoresist was developed to make alignment of the second layer easier. The first layer was finished by rinsing the wafer with deionized water and isopropyl alcohol (IPA).

To create the taller mixing channels and observation channels, photolithography was repeated to create a second 85-micron layer that was applied on top of the 15-micron layer. SU-8 2050 (SU-8 2050, MicroChem Corp) was used for the photoresist. The same photolithography steps were taken for the second layer as for the first layer, which included the soft-bake, the alignment, the UV-light exposure, the post-bake, and the development. Four alignment marks were placed in the four corners on the photolithography masks to aid in the alignment of the two photolithography layers (See Appendix B). Once the second layer was complete, we had a wafer with a dual-height pattern of microchannels that was used as a mold for the soft lithography process.

We performed soft lithography by pouring a silicon elastomer, PDMS (polydimethylsiloxane, PDMS; Dow Corning) mixed with cross linking agent (10:1 ratio by

weight) onto the wafer mold. The PDMS was placed in a vacuum chamber for ten minutes each immediately before and after pouring it over the wafer to remove bubbles. Any remaining bubbles were then removed by applying pressurized air directly to the bubbles. The PDMS was cured for a minimum of one hour at 65°C. The PDMS was then manually cut out from the wafer mold, and the inlet and outlet holes were punched into the PDMS. To complete the device, the PDMS was bonded to a glass slide (25 mm x 75 mm x 1 mm) via plasma bonding (Plasma Etch, Inc.) and heated for one hour at 95°C. In some cases, the buffer inlet manifold collapsed during the bonding process. This issue was avoided by gently placing the PDMS onto the glass slide as opposed to pressing the PDMS down onto the glass slide.

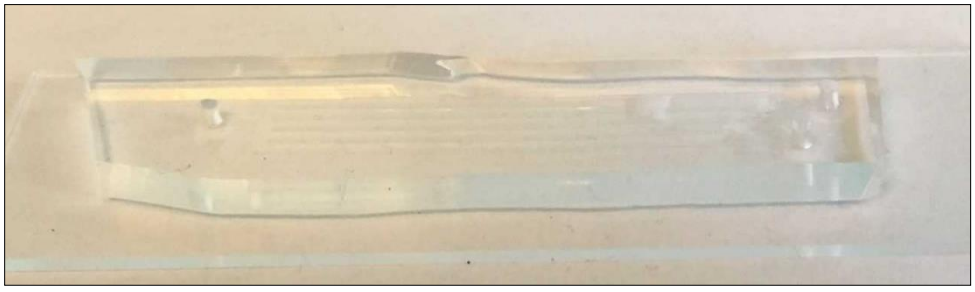

Figure 8: The completed single-height serial dilution module. The glass slide of the device is 25 mm x 75 mm x 1 mm.

5.0 Serial Dilution Device Validation Testing

5.1 Validation Test Setup

We performed a validation test using particle tracking to verify that the serial dilution device produced the necessary flow rates to create the desired concentrations, 1, 10^{-1}, 10^{-2}, 10^{-3}, and 10^{-4}. This validation test focused on the flow rates at the bridge and mixing channel junctions on the inlet side of the device (P4, P7, P10, P13 shown in Fig. 7). Because the double lithography was

unsuccessful, a single-height version of the device with 15-micron high mixing channels was tested.

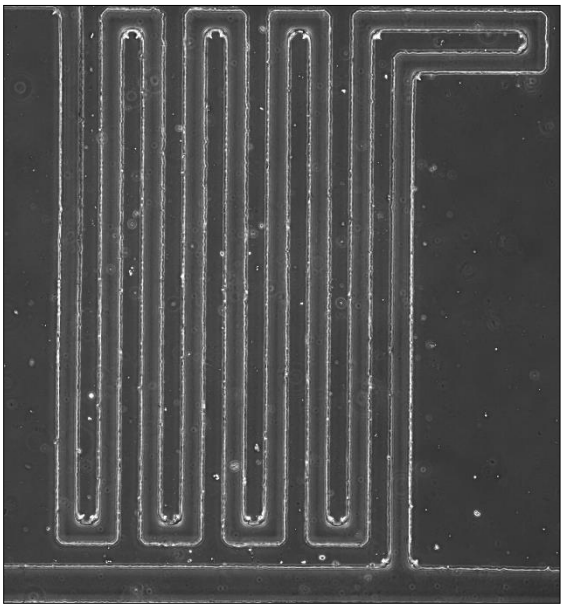

Figure 8: Closeup of a microchannel within the device (first single-layer photolithography device). The channel width is 50 microns in this version of the device.

A solution of 0.5-micron diameter fluorescent tracer particles were placed in both inlets of the device. The serial dilution device was designed to operate at 100 kPa for both inlet pressures. However, because the mixing channels were the incorrect height, the resistance of the mixing channels were too high, causing a change in the flow rates at the given inlet pressures of 100 kPa. For testing purposes, junction P13 was used to calibrate the inlet pressures. The pressure applied to each inlet was adjusted until the two flow streams entering P13 were approximately flowing in at a 9:1 ratio. From there, videos of each mixing channel junction were recorded. The particles in the flow streams were tracked using custom Matlab codes and the speeds of each channel entering and exiting each junction were found.

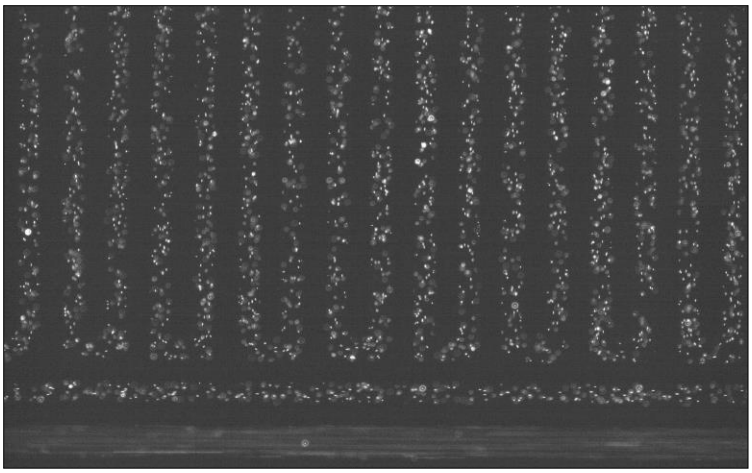

Figure 9: Closeup of microchannels with 0.5-micron fluorescent particles seeded in the media for particle tracking. The channel width of this version of the device (first single-layer photolithography device) is 50 microns.

5.2 Results and Analysis

The flow speeds of each channel at each mixing junction were plotted. The dilution ratio was plotted separately and was calculated by dividing the flow speed of the 10% inlet (chemical-side inlet) by the flow speed of the junction outlet (flow speed within the mixing channel). The results of the validation test are shown in Fig. 10.

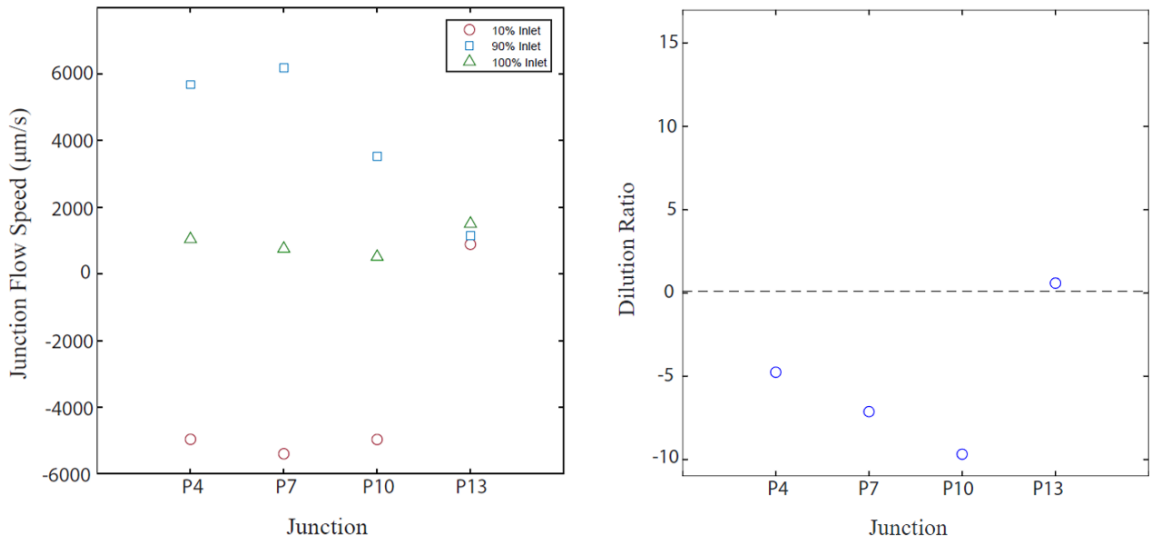

Figure 10: Validation test results with the flow speed of each channel at each mixing channel junction (right) and the dilution ratio at each mixing channel junction (left) (credit: Michael Stehnach).

The negative values within the plots signify backflow in which the flow was traveling in the opposite direction intended. The high resistance mixing channels redirected flow back out the inlet channels, causing the chemical-side inlet channels (10% inlets) to have backflow. The target dilution ratio for the device is 0.1, represented by the dotted line in Fig. 10. Only the mixing junction that was used for calibration was around the 0.1 dilution ratio. The 10% inlet backflow at all the other mixing junctions correlates with negative dilution ratio results.

The results were as expected for a single-layer photolithography version of the serial dilution module. Since the mixing channel heights were 15 microns instead of the intended height 100 microns, the mixing channel resistances were nearly 50 times the intended resistances of the mixing channels. The extra resistance in the mixing channels diverted more of the flow away from the mixing channels towards other connected channels, drastically altering the flow rates. The effects of the high resistance mixing channels on the flow rates was predicted with the mathematical theory we have used to design the device. The agreement between the test results and our mathematical theory is a positive sign that a device with the dimensions we calculated for the two-layer photolithography design may function properly.

6.0 Conclusions and Future Work

The development of new rapid screening technologies is crucial to the advancement of microbial ecology. In this work, we have taken key steps toward the design and fabrication of a multiplexing microfluidic device for microbial chemotaxis assays. In particular, we successfully designed a serial dilution microchannel using hydraulic circuit analysis, and we fabricated a first version of the microchannel. However, the performance of the device was

severely hampered by problems in the microfabrication of the two-layer microfluidic device. Since we were unable to align the photolithography masks during the two-layer photolithography, the designed device was unable to be fabricated or tested. The mask aligner had insufficient resolution to accurately align the second layer of the mixing channels to the first layer. As a result, the unaligned top layer merged channels together that were not intended to be connected.

The validation testing of the single-layer photolithography device concluded that backflow was produced in most of the device mixing junctions due to the high resistance of the 15-micron tall mixing channels. Validation test results of the single photolithography layer were as expected, which suggests that our theory used for calculating the proper device dimensions are correct.

To make the two-layer photolithography fabrication procedure more feasible, adjustments can be made to the photolithography mask design. Additional alignment marks can be placed on the mask near the mixing channels to aid in mask alignment. The mixing channels should also be fabricated with a single 100-micron layer, rather than with a 15-micron layer and an 85-micron layer stacked on top of each other. In other words, one 15-micron photolithography layer should create all the 15-micron channels and the second 100-micron photolithography layer should create all the 100-micron channels. Additionally, the ends of the 15-micron channels that connect to a mixing channel should be altered to have wider channel ends by designing a wide rectangular reservoir at the end of the channel. The wider channel ends would provide a bigger target for the mixing channel ends which would create more room for error when lining up the mixing channel ends to the 15-micron-tall channel ends.

A possible alternative to the diffusion mixing channels is to replace them with herringbone mixing channels, a channel with a chevron pattern imprinted into the channel walls[35]. If incorporated into the next iteration of our dilution channel design, this herringbone mixing channel would have a more efficient mixing time and shorter mixing length. However, creating the chevron channels would still require the two-layer photolithography process.

With these modifications, the dual-height serial dilution device will be possible to fabricate. The predictable results of the validation testing of the single-layer photolithography module suggests that with the proper two-layer photolithography fabrication, the serial dilution module will be able to create the desired concentrations.

Once a validated serial dilution module is created, it will be ready to be integrated into a chemotaxis serial dilution device. Creating the complete chemotaxis serial dilution device requires adding an additional inlet for the bacteria and channels connecting the inlet to the observation channels. The resulting device will be able to perform 6 "T-junction" chemotaxis assays of several different concentrations at once.

Future work also includes automating the microscope for the testing process so that multiple replicates may be performed with minimal human interaction. With the completed serial dilution device and automated microscopy, efficiently performing hundreds of chemotaxis assays will be possible. The device will not only be helpful in speeding up ecology and environmental science, but also in the pharmaceutical industry and infectious disease research.

7.0 References

1. Wilkinson, P. C. (1998). Encyclopedia of Immunology (second edition). *Science Direct.* 533-537.
2. Bacterial Chemotaxis. (2016). Retrieved from https://www.ks.uiuc.edu/Research/chemotaxis/
3. Stocker, R. & Seymour, J. R. (2019). *Microbiology and Molecular Biology Reviews. 76,* 792-812.
4. The Carbon Cycle. (2007). *NESTA.* Retrieved from scied.ucar.edu/carbon-cycle.
5. Bernhard, A. (2010). The nitrogen cycle: processes, players, and human impact. Retrieved from https://www.nature.com/scitable/knowledge/library/the-nitrogen-cycle-processes-players-and-human-15644632
6. Gillespie, C. (2018). Why is nitrogen important for living things? Retrieved from https://sciencing.com/why-nitrogen-important-living-things-4609019.html
7. Jacob, R. & Cordaro, E. (2000). *RPI.* Retrieved from https://www.rpi.edu/dept/chem-eng/Biotech-Environ/Projects00/biotreat/nitrification.html
8. Lehnert, N., Dong, H. T., Harland, J. B., & Hunt, A. P. (2018). Reversing nitrogen fixation. *Nature Reviews Chemistry. 2,* 278-289.
9. Lin, B. & Levchenko, A. (2015). Spatial manipulation with microfluidics. *Frontiers Bioengineering and Biotechnology. 3,* 39.
10. Hattori, K., Sugiura, S. & Kanamori, T. (2009). Generation of arbitrary monotonic concentration profiles by a serial dilution microfluidic network composed of microchannels with a high fluidic-resistance ratio. *Lab on a Chip. 9,* 1763 – 1772.

11. Oh, K. W., Lee, K., Ahn, B. & Furlani, E. P. (2011). Design of pressure-driven microfluidic networks using electric circuit analogy. *Lab on a Chip. 12,* 515-545.

12. Bruus, H. (2008). Hydraulic Resistance and Compliance. In *Theoretical Microfluidics*. *Oxford University Press, 71-76.*

13. Microfluidic mixing. *Massachussetts Institute of Technology.* Retrieved from https://ocw.mit.edu/courses/mechanical-engineering/2-674-micro-nano-engineering-laboratory-spring-2016/readings/

14. Kamimura, Y., Cai, H. & Devreotes, P. N. (2010). 6 – TORC2 and chemotaxis in dictyostelium discoideum. *ScienceDirect. 28,* 125 -142.

15. Walker, G. M., Monteiro-Riviere, N., Rouse, J. & O'Neill, A. T. (2006). A linear dilution microfluidic device for cytotoxicity assays. *Lab on a Chip. 7,* 226-232.

16. Saadi, W., Wang, S. J., Lin, F. & Jeon, N. L. (2006). A parallel-gradient microfluidic chamber for quantitative analysis of breast cancer cell chemotaxis. *Biomedical Mirodevices. 8,* 109-118.

17. Merriam-Webster. (2019). Chemoattractant Medical Definition. Retrieved from www.merriam-webster.com/medical/chemoattractant.

18. Zicha, D., Dunn, G. A., & Brown, A. F. (1991). A new direct-viewing chemotaxis chamber. *Journal of Cell Science. 99,* 769-775.

19. Photolithography Basics. Retrieved from https://static1.squarespace.com/static/57b26cc76b8f5b7524bf9ed2/t/57f97113725e25a7b5dd0907/1475965203340/

20. Casquillas, G. V. Introduction about Soft-Lithography for Microfluidics. *Elveflow*, Retrieved from www.elveflow.com/microfluidic-tutorials/soft-lithography-reviews-and-

tutorials/introduction-in-soft-lithography/introduction-about-soft-lithography-and-polymer-molding-for-microfluidic/.

21. Benesch-Lee, F., Guevara, J. M. L. & Albrecht, D. R. (2017). Multilayer photolithography with manual photomask alignment. *RSC Internet Services.* Retrieved from http://blogs.rsc.org/chipsandtips/2017/06/05/multilayer-photolithography-with-manual-photomask-alignment/

22. Stocker, R. & Seymour, J. R. (2012). Ecology and physics of bacterial chemotaxis in the ocean. *MMBR. 74,* 812-992.

23. Chisholm, S. W. (2019). Stirring times in the Southern Ocean. Retrieved from https://www.nature.com/articles/35037696

24. The marine nitrogen cycle. (2016, January 05). Retrieved from https://wordsinmocean.com/2012/02/21/the-marine-nitrogen-cycle/

25. Christian, J. R. & Anderson, T. R. (2002). Biogeochemistry of Marine Dissolved Organics Matter. *Academic Press,* 717-755.

26. Glogauer, M. (2012). Goldman's Cecil Medicine (Twenty-Fourth Edition). *Elsevier, 1,* 1111-1118.

27. Englert, D. L., Manson, M. D. & Jayaraman, A. (2009). Flow-based microfluidic device for quantifying bacterial chemotaxis in stable, competing gradients. *American Society of Microbiology, 75,* 4557-4564.

28. Si, G., Yang, W., Bi, S., Luo, C. & Ouyang, Q. (2012). A parallel diffusion-based microfluidic device for bacterial chemotaxis analysis. *Lab on a Chip, 12,* 1389-1394.

29. Shen, C., Xu, P., Cai, D., Liu, S. & Du, W. (2014). Bacterial chemotaxis on SlipChip. *Lab on a Chip. 14,* 3074-3080.

30. Middelboe, M., Riemann, L., Steward, G. F., Hansen, V., and Nybroe, O. (2003). Virus-induced transfer of organic carbon between marine bacteria in a model community. *Aquatic Microbial Ecology, 33,* 1-10

31. Successive Serial Dilution. (2003). *Five Colleges of Ohio.* Retrieved from http://biology.kenyon.edu/courses/biol09/tetrahymena/serialdilution3.htm

32. "Conservation of Mass". (2015). *National Aeronautics and Space Administration*. Retrieved from https://www.grc.nasa.gov/www/k-12/airplane/mass.html

33. Wang, G. R., Yang, F. & Zhao, W. (2014). There can be turbulence in microfluidics at low Reynolds number. *Lab on a Chip, 14,* 1452.

34. Engineering ToolBox. (2003). Reynolds Number. Retrieved from https://www.engineeringtoolbox.com/reynolds-number-d_237.html

35. Stroock, A. D., Dertinger, S. K. W., Ajdari, A., Stone, H. A. & Whitesides, G. M. (2002). Chaotic mixer for microchannels. *Science, 295,* 647-651.

36. Shen, C., Xu, P., Huang, Z., Cai, D., Liu, S. & Du, W. (2014). Bacterial chemotaxis on SlipChip. *Lab on a Chip, 14,* 3074-3080.

Appendices

Appendix A: Matlab Codes

1. Flow Rate Matrix and Resistance Calculations Matlab Code

```
%%Q
q0 = 10; % observation channel flow rate [microliters/min]
q0 = q0/60; %[microliters/s]
A = [0, 9, -1, 0, 0, 0, 0, 0, 0, 0, 0, 0, 0; ...
    0, 0, 0, 0, 9, -1, 0, 0, 0, 0, 0, 0, 0;...
    0, 0, 0, 0, 0, 0, 0, 9, -1, 0, 0, 0, 0;...
    0, 0, 0, 0, 0, 0, 0, 0, 0, 0, 9, -1, 0;...
    1, -1, 0, 0, 0, 0, 0, 0, 0, 0, 0, 0, 0;...
    0, 0, 0, 1, -1, 0, 0, 0, 0, 0, 0, 0, 0;...
    0, 0, 0, 0, 0, 0, 1, -1, 0, 0, 0, 0, 0;...
    0, 0, 0, 0, 0, 0, 0, 0, 0, 1, -1, 0, 0;...
    0, 0, -1, 0, 0, -1, 0, 0, -1, 0, 0, -1, 1;...
    0, 1, 1, -1, 0, 0, 0, 0, 0, 0, 0, 0, 0;...
    0, 0, 0, 0, 1, 1, -1, 0, 0, 0, 0, 0, 0;...
    0, 0, 0, 0, 0, 0, 0, 1, 1, -1, 0, 0, 0;...
    0, 0, 0, 0, 0, 0, 0, 0, 0, 0, 1, 1, 0];

B = [0; 0; 0; 0; q0; q0; q0; q0; q0; 0; 0; 0; q0];
%X = [q01; q04; q11; q12; q14; q21; q22; q24; q31; q32;
q34; q41; q1]

Q = A\B %[microliter/s]

q01 = Q(1); %[microliters/s]
q04 = Q(2);%[microliters/s]
q11 = Q(3);%[microliters/s]
q12 = Q(4);%[microliters/s]
q14 = Q(5);%[microliters/s]
q21 = Q(6); %[microliters/s]
q22 = Q(7); %[microliter/s]
q24 = Q(8); %[microliter/s]
q31 = Q(9); %[microliters/s]
q32 = Q(10);%[microliters/s]
q34 = Q(11);%[microliters/s]
q41 = Q(12);%[microliters/s]
q1 = Q(13); %[microliters/s]

%% Resistances
% 6 concentration - simplified matrix
 % The top two branches were solved by hand.
```

```
 R0 = 0.0003; % [mPa-s/μm^3]
 PL = q0 * R0; %kPa
 P4 = PL; %kPa

 % Identify Knowns
 P1 = 10; %kPa
 P2 = 10; %kPa

 %Calculate
 R1 = (P1 - PL)/q0; % [kg/m^4/s]
 R2 = (P1 - P4)/q12; % [kg/m^4/s]

 % Resistance Values
 R33 = 0.3600; % [mPa-s/μm^3]
 R23 = 0.371; % [mPa-s/μm^3]
 R13 = 0.3821; % [mPa-s/μm^3]
 R03 = 0.3932; % [mPa-s/μm^3]

%Convert Units
 R0 = R0 * 10e-6; % [kg/mm^4/s]
 R33 = R33 * 10e-6; % [kg/mm^4/s]
 R23 = R23 * 10e-6; % [kg/mm^4/s]
 R13 = R13 * 10e-6; % [kg/mm^4/s]
 R03 = R03 * 10e-6; % [kg/mm^4/s]

 A = [0, 1, 0, 0, 0, 0, 0, 0, -q34, 0, 0, 0; ...
      0, 0, 0, 0, 1, 0, 0, 0, 0, 0, 0, 0; ...
      0, 0, q31, 0, 1, 0, 0, 0, 0, 0, 0, 0; ...
      0, 0, 0, q21, 0, 1, 0, 0, 0, 0, 0, 0; ...
      0, 0, 0, 0, -1, 1, 0, 0, 0, -q24, 0, 0; ...
      0, 0, 0, 0, 0, 1, 0, 0, 0, 0, 0, 0; ...
      0, q11, 0, 0, 0, 0, 1, 0, 0, 0, 0, 0; ...
      0, 0, 0, 0, 0, -1, 1, 0, 0, 0, -q14, 0; ...
      0, 0, 0, 0, 0, 0, 1, 0, 0, 0, 0, 0; ...
      0, 0, 0, 0, 0, 0, -1, 1, 0, 0, 0, -q04; ...
      q01, 0, 0, 0, 0, 0, 0, 1, 0, 0, 0, 0; ...
      0, 0, 0, 0, 0, 0, 0, 1, 0, 0, 0, 0];
  B = [P4; PL + R33 * q0; P1; P1; 0; PL + R23 * q0; P1; 0;
PL + R13 * q0; ...
       0; P2; PL + R03 * q0];

 PR = A\B

%% Q (check)
close all; clear all; clc;
a = 1/10; %Q_bridge / Joining Channel (i.e. q04/q12 = a)
```

```
% Calculate Flow Rate:
q0 = 1.2; %[microL/min]
q0 = q0*1E9/60; % [micron^3/s]

q41 = q0*(1-a);     % [micron^3/s]
q32 = q0*(1+a);     % [micron^3/s]
q31 = q32*(1-a);    % [micron^3/s]
q22 = q0+(a*q32);   % [micron^3/s]
q21 = q22*(1-a);    % [micron^3/s]
q12 = q0+(a*q22);   % [micron^3/s]
q11 = q12*(1-a);    % [micron^3/s]
q01 = q0 + (a*q12); % [micron^3/s]

q04 = a*q12;        % [micron^3/s]
q14 = a*q22;        % [micron^3/s]
q24 = a*q32;        % [micron^3/s]
q34 = a*q0;         % [micron^3/s]
%% Check Flow Rates
Check(1) = (q41+q34)/q0;
Check(2) = (q34+q0)/q32;
Check(3) = (q31+q24)/q32;
Check(4) = (q24+q0)/q22;
Check(5) = (q14+q21)/q22;
Check(6) = (q14+q0)/q12;
Check(7) = (q11+q04)/q12;
Check(8) = (q04+q0)/q01;

%% Hattori flow rate calculations
% C0 = 1; % initial concentration
% Cinf= 0; % buffer
% a = 0.1; %dilution factor
% k = 0:N;
% C = C0*a.^(0.5*k);
% C = [C Cinf];


%% Resistances (check)
% Julia Noble 2/19/19
%Input flow rates, bridge resistance, R43, inlet pressure
and
% # of concentrations (k).
%Outputs R1 (Left hand side resistances) and R3
%(right hand side resistances) in the form of vectors R1
and R3
%respectively.
```

```
%q vectors - flow rates solved previously:
qVec1 = [q01 q11 q21 q31 q41 q0]; %[micron^3/sec]
qVec2 = [q0, q12, q22, q32, q0, q0];
qVec4 = [q04, q14, q24, q34];
%all q3's are equal to q0

% %convert units
% qVec1 = qVec1 * 60; %[micron^3/min]
% qVec2 = qVec2 * 60; %[micron^3/min]
% qVec4 = qVec4 * 60; %[micron^3/min]

%Givens
R4 = 0.17; % bridge resistance
Pin = 10000000; %mPa

k = 5; %number of concentrations
R1 = zeros([6 1]);
R3 = zeros([5 1]);
R1(k+1) = Pin/q0;
R3(k) = 0; %RN3 %R43

while k > 1

    %Solving for left hand side resistances
    R1(k) = (Pin - q0*R3(k))/qVec1(k);
    k = k-1; %Move to next branch
    %Solving for right hand side resistances
    R3(k) = (qVec4(k)*R4+q0*R3(k+1))/q0;

end

%Solving for R01
R1(1) = (Pin - q0*R3(1))/qVec1(1)

R3
```

2. Verifying Hattori's Flow Rate and Hydraulic Resistance Equations Using Hattori's Paper Conditions Matlab Code (Eq. 10, 11)

```
%% Given - Hattori Paper Conditions
 {
 p1 = 20;         % [kPa] inlet channels
 Q0 = 1.2;        % [ul/min] each test channel
 a = 0.1;         % dilution scale
 N = 10;          % dilution steps
 C0 = 1;          % initial concentration
 Cinf = 0;        % buffer concentration
```

```
 Rc = 0.17;      % [mPa-s/um^3] set connector channel
resistance
 R0 = 0;         % [mPa-s/um^3] set second to last outlet
channel resistance

% Units
 p1 = p1*1000^2;
 Q0 = Q0/60*1000^3;
 k = 0:N;
 C = C0*a.^(0.5*k);
     C = [C Cinf]';
 }

     %% flow rates
Q3 = Q0*ones(N+1,1);

Q4 = zeros(N,1);
for kk = 0:(N-1)
    dummy = 0;
    for ii = (kk+1):N
        dummy =  (C(ii+1)/C(kk+1+1)) * Q0 + dummy;
    end
    Q4(kk+1) = (C(kk+1+1)/C(kk+1)) * dummy;
end

Q2 = zeros(N+1,1);
for kk = 0:N
    dummy = 0;
    for ii = kk:N
        dummy =  (C(ii+1)/C(kk+1)) * Q0 + dummy;
    end
    Q2(kk+1) = dummy;
end

Q1 = zeros(N,1);
for kk = 1:N
    dummy = 0;
    for ii = kk:N
        dummy =  (C(ii+1)/C(kk+1)) * Q0 + dummy;
    end
    Q1(kk+1) = (C(kk-1+1)-C(kk+1))/C(kk-1+1) * dummy;
end
Q1(N+1+1) = Q0;
Q1(0+1) = Q3(0+1)+Q4(0+1);

%{
% check 1
```

```
Q3(1:N-1)+Q4(1:N-1)-Q2(1:N-1)
[Q3(1:N-1) Q4(1:N-1) Q2(1:N-1)]

% check 2
Q4(1:N-1)+Q1([1:N-1]+1)-Q2([1:N-1]+1)
[Q4(1:N-1) Q1([1:N-1]+1) Q2([1:N-1]+1)]
%}

% check 3 - dilution ratio
%Q4(1:N)./(Q1(2:N+1)+Q4(1:N))

%% Resistances
R1 = 0*Q1;
R2 = 0*Q2; % Stays as zero
R3 = 0*Q3;
R4 = Rc*ones(size(Q4));

R3(N+1) = R0;
for kk = (N-1):-1:0
    R3(kk+1) = (Q4(kk+1)*R4(kk+1) +
Q3(kk+1+1)*R3(kk+1+1))/Q3(kk+1);
end

for kk = 0:N
    R1(kk+1) = (p1 - Q3(kk+1)*R3(kk+1))/Q1(kk+1);
end
R1(N+1+1) = p1 / Q1(N+1+1);

%% more checks
R1
R3
%R1: R01, R11, R21, R31, R41, R51
%R3: R03, R13, R23, R33, R43 (R0)
```

3. Our Flow Rate and Hydraulic Resistance Calculations Using Hattori Equations (Eq. 10, 11) Matlab Code

```
%% Given - Our Conditions

p1 = 1;         % [kPa] inlet channels
Q0 = 1;        % [ul/min] each test channel
a = 0.1;         % dilution scale
N = 4;          % dilution steps
C0 = 1;          % initial concentration
Cinf = 0;        % buffer concentration

Rc = 0.1;       % [mPa-s/um^3] set connector channel
resistance
```

```
R0 = 0.35;    % [mPa-s/um^3] set second to last outlet
channel resistance

k = 0:N;
C = C0*a.^(k);
    C = [C Cinf]';

%% flow rates
Q3 = Q0*ones(N+1,1);

Q4 = zeros(N,1);
for kk = 0:(N-1)
    dummy = 0;
    for ii = (kk+1):N
        dummy =  (C(ii+1)/C(kk+1+1)) * Q0 + dummy;
    end
    Q4(kk+1) = (C(kk+1+1)/C(kk+1)) * dummy;
end

Q2 = zeros(N+1,1);
for kk = 0:N
    dummy = 0;
    for ii = kk:N
        dummy =  (C(ii+1)/C(kk+1)) * Q0 + dummy;
    end
    Q2(kk+1) = dummy;
end

Q1 = zeros(N,1);
for kk = 1:N
    dummy = 0;
    for ii = kk:N
        dummy =  (C(ii+1)/C(kk+1)) * Q0 + dummy;
    end
    Q1(kk+1) = (C(kk-1+1)-C(kk+1))/C(kk-1+1) * dummy;
end
Q1(N+1+1) = Q0;
Q1(0+1) = Q3(0+1)+Q4(0+1);

%{
% check 1
Q3(1:N-1)+Q4(1:N-1)-Q2(1:N-1)
[Q3(1:N-1) Q4(1:N-1) Q2(1:N-1)]

% check 2
Q4(1:N-1)+Q1([1:N-1]+1)-Q2([1:N-1]+1)
[Q4(1:N-1) Q1([1:N-1]+1) Q2([1:N-1]+1)]
```

```
%}

% check 3 - dilution ratio
%Q4(1:N)./(Q1(2:N+1)+Q4(1:N))

%% Resistances
R1 = 0*Q1;
R2 = 0*Q2; % Stays as zero
R3 = 0*Q3;
R4 = Rc*ones(size(Q4));

R3(N+1) = R0;
for kk = (N-1):-1:0
    R3(kk+1) = (Q4(kk+1)*R4(kk+1) +
Q3(kk+1+1)*R3(kk+1+1))/Q3(kk+1);
end

for kk = 0:N
    R1(kk+1) = (p1 - Q3(kk+1)*R3(kk+1))/Q1(kk+1);
end
R1(N+1+1) = p1 / Q1(N+1+1);

%% more checks
R1
R3
%R1: R01, R11, R21, R31, R41, R51
%R3: R03, R13, R23, R33, R43 (R0)
```

4. Channel Dimension Calculations Matlab Code (Eq. 12, 17)

```
% microfluidic resistance calculator for rectangular
channels
% Julia Noble 10/24/18

%% calculate length based on resistance, width, and height
clear

%Define Variables
r = [0.1000
0.5461
0.618
0.6296
0.6465
0.7222
0.9997
0.3929
0.3818
```

```
0.3707
0.3597
0.3497]; %[mPa-s/um^3] vector of resistances
r = r.*1e15; %[Pa/m^3]
h = 15e-6; %[m]
w = 50e-6; %[m]
v = 1e-3; % [Pa-s] water

S = 0;
addSum = 1;
n = (1:2:500);
k = 1;
for k = 1:length(n)
    addSum = (1/n(k).^5)*tanh(n(k)*pi*w./(2*h));
    S=addSum+S;
    k = k+1;
end

A = (S * 192/pi^5) * (h/w);
p = zeros(length(r), 1); % Create empty vector
i = 0;
for i = 1:length(r)
    L = r(i).*(1-A)*w*(h^3)/(12*v);% m
    L = L * 1e3; % mm
    p(i) = L %vector of lengths
end

%% calculate resistance from dimensions (for mix channels)
clear

%Define Variables
h = 100e-6; %[m]
w = 750e-6; %[m]
v = 1e-3; % [Pa-s] water
L = 15e-3; % m

S = 0;
addSum = 1;
n = (1:2:500);
k = 1;
for k = 1:length(n)
    addSum = (1/n(k).^5)*tanh(n(k)*pi*w./(2*h));
    S=addSum+S;
    k = k+1;
end

A = (S * 192/pi^5) * (h/w);
```

```
r = 1/(1-A) * 12*v*L/(w*h^3); %{Pa.s/m^3)
resistance = r*1e-15 %[mPa.s/um^3]


%% Estimate (check) of Resistance (eq. 17)
L = .025e-3; %length (m)
h = 15e-6; %height (m)
w = 50e-6; %width (m)
v = 1e-3; %water (Pa.s)

resistance = (12*L*v/(1-0.63*h/w))*(1/(w*h^3)); %Pa.s/m^3
%convert to mPa.s/um^3
resistance = resistance*1e-15
```

5. Mixing Channel Length Calculation Matlab Code (Eq. 13, 14, 15, 16)

```
%Calculates required mix length

%Define Our Conditions
D = 5.62e-10; % [m^2/s] from Hattori for calcein with
molecular weight 623 Da
w = 50; %[microns]channel width
h = 100; %[microns] channel height
q = 1.1111; %[ul/min] flow speed

% Change Units
w = w*1e-6; % [meters]
h = h*1e-6; % [meters]
q = q*(1e-9)/60; % [m^3/sec]

%Calculate Channel Length
dt = (w^2)/D; % mix
u = q/(h*w); % average flow speed
L = u*dt; % mixing length [meters]
L = L*1e6 % convert to microns
```

Appendix B: Photolithography Masks

First Set of Single-Layer Photolithography Mask Design (AutoCAD drawings)

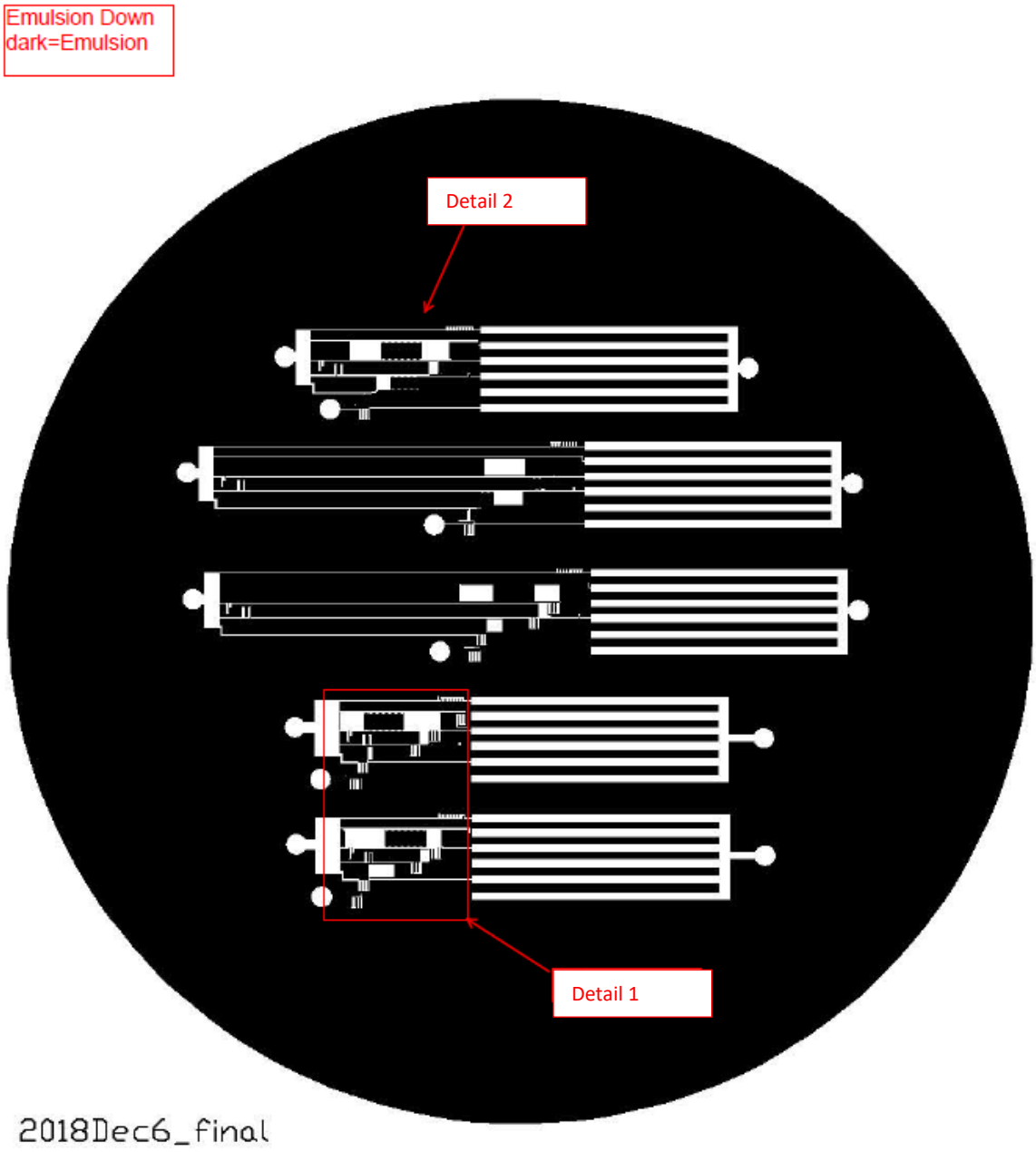

Figure a: Full set of mask designs of the first single-layer photolithography designs (AutoCAD drawing). This was used for fabrication of five variations of the first single-layer photolithography design.

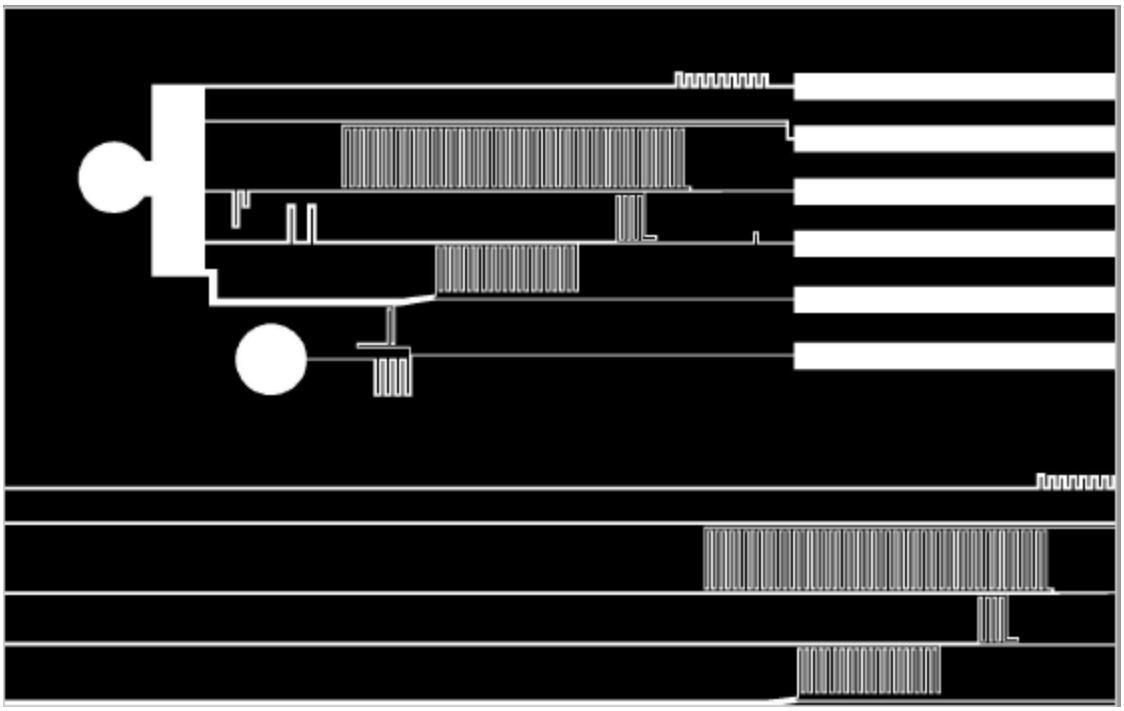

Figure b: Detail 1 closeup of mask design (AutoCAD drawing).

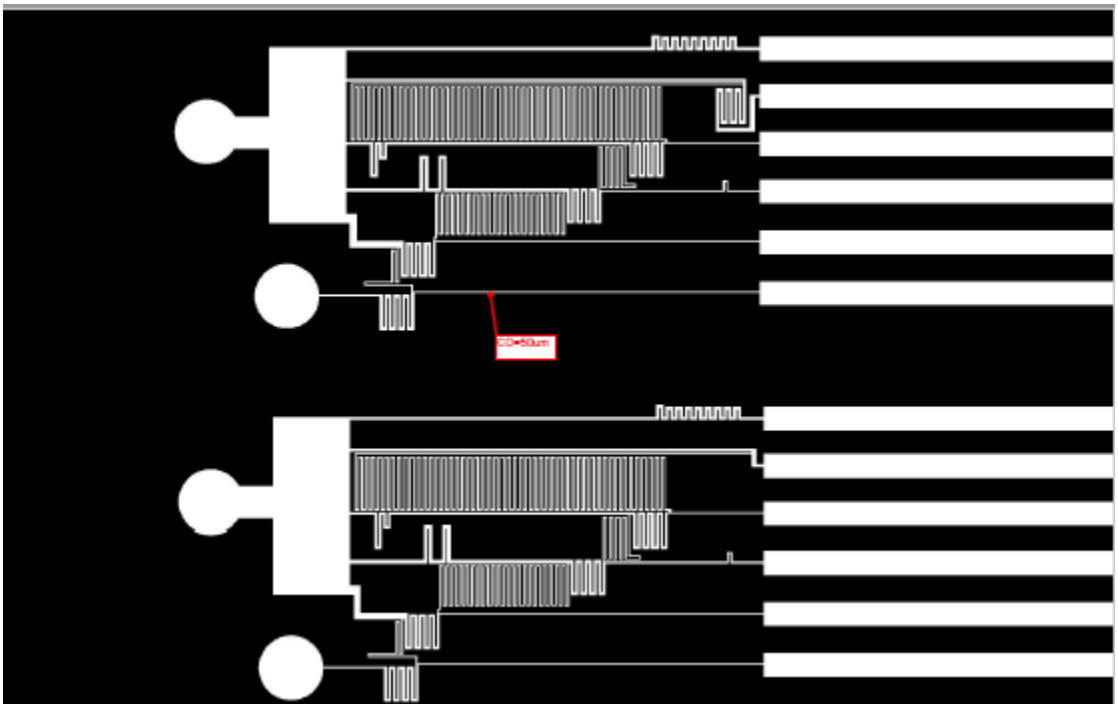

Figure c: Detail 2 closeup of mask design (AutoCAD drawing).

Double-Layer Photolithography Mask Design (AutoCAD drawings)

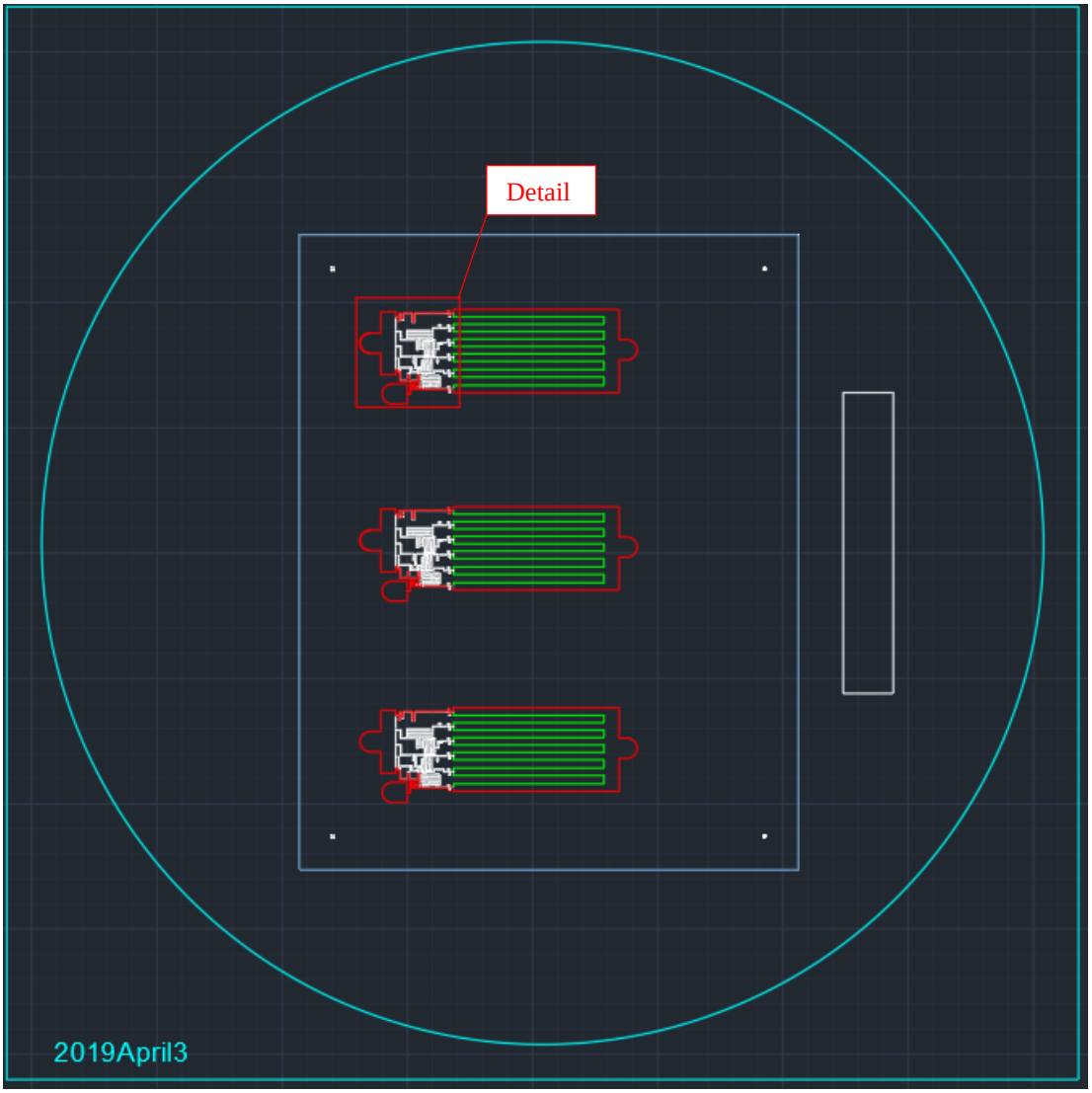

Figure d: First layer mask of the double-layer photolithography design (AutoCAD drawing). This was used for fabrication of three identical double-layer photolithography devices.

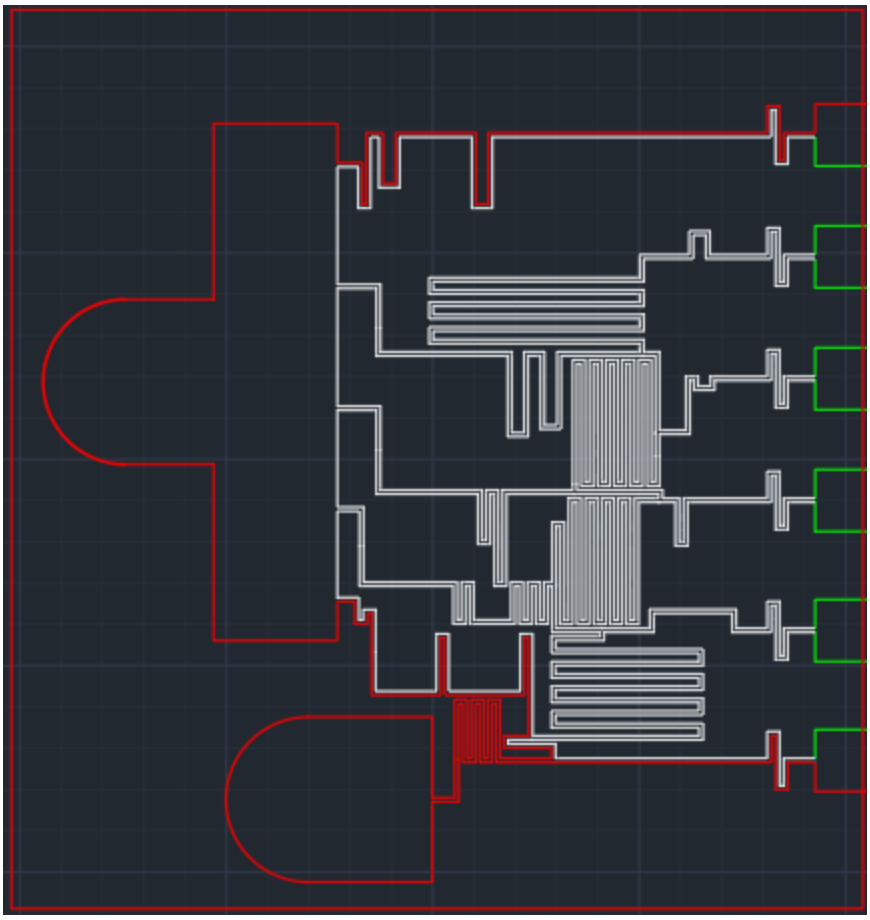

Figure e: Detail of the first layer mask of the double-layer photolithography design (Fig. d) (AutoCAD drawing).

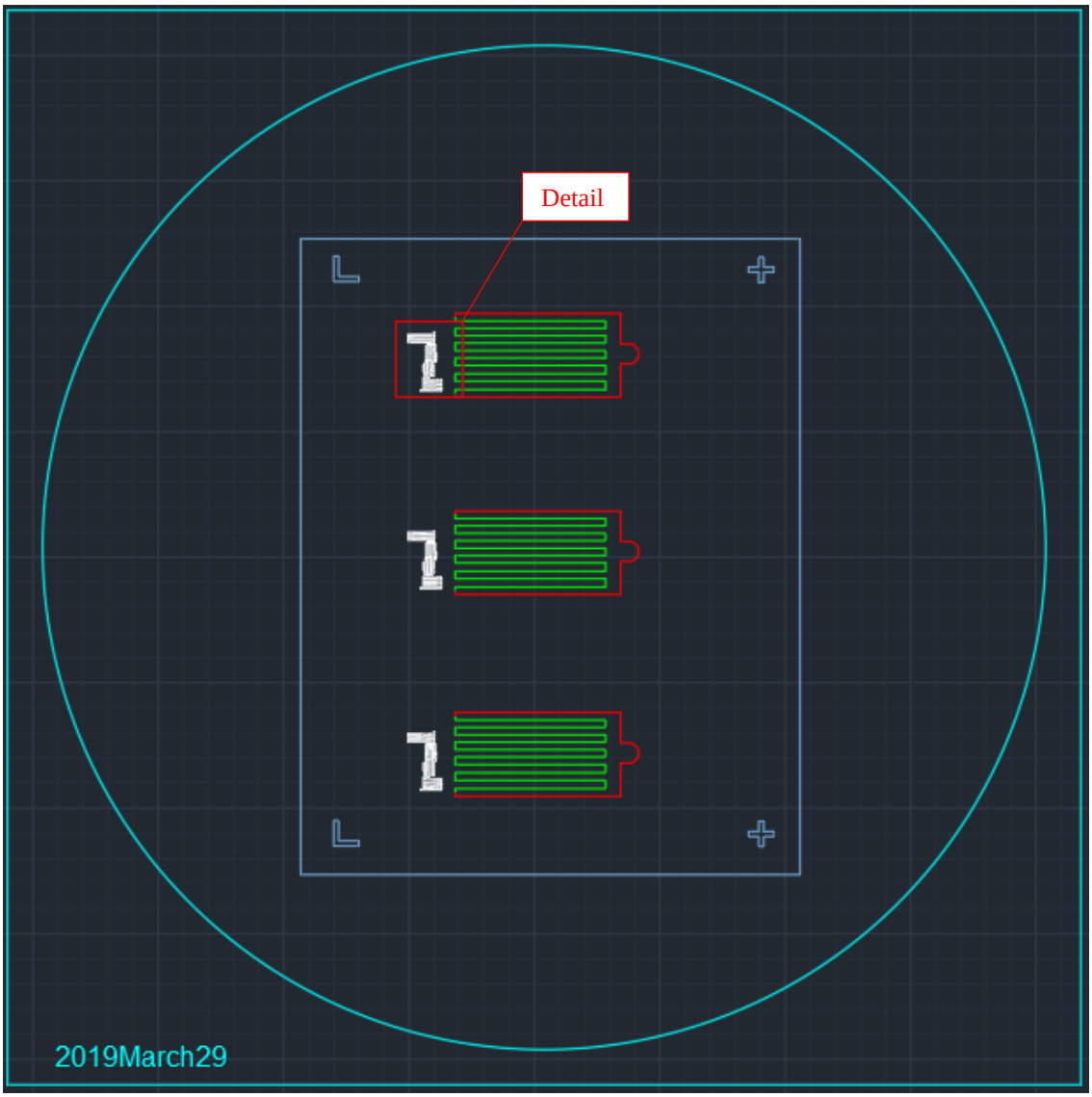

Figure f: Second layer mask of the double-layer photolithography design (AutoCAD drawing). This was used for fabrication of three identical double-layer photolithography devices.

Figure g: Detail of the second layer mask of the double-layer photolithography design (Fig. f).